Machine Learning Predicts Failure in Sandstone Analog using Critical Point Indicators

Harsh Biren Vora and Julia K. Morgan

Department of Earth, Environmental, and Planetary Sciences, Rice University, Houston, TX 77006

Corresponding Author: Harsh Biren Vora (hv6@rice.edu)

Key Points:

- Microcracking rate, mode, location and seismic moment document temporal variations as prior to critical failure in sandstone analog
- Temporal trends of precursory indicators can predict critical failure using machine learning over a range of confining pressures
- Integrated analysis using multiple independent precursors improves robust failure prediction capability

Abstract

We analyze precursors of critical failure in Discrete Element simulations of biaxial tests on sandstone and employ machine learning to predict failure. We document four dimensionless indicators from emergent microcrack growth: microcracking variance, fraction of shear to total microcracks, fractal dimension of microcrack hypocenters, and slope of the frequency-magnitude moment distribution. Each indicator documents distinct time-to-failure characteristics, and we employ them as inputs for a neural network to predict critical failure. Over confining pressures of 0-50 MPa, our neural network predicts time-to-failure and stress-to-failure well (R^2=0.84 and 0.94 respectively), revealing that all four deformation indicators contribute to failure prediction. Thus, we document a suite of precursory indicators of failure in cohesive rock material and show that they can predict failure using machine learning. Our approach can be applied to seismic data from the laboratory to earthquake sequences and may lead to advances in short-term failure forecasting techniques.

Plain Language Summary

The prediction of earthquake timing and magnitude is of fundamental interest to geoscientists. For decades, researchers have tried to understand the physics behind earthquakes through laboratory deformation experiments, where fractures grow through the coalescence of microcracks. We simulate laboratory deformation experiments on a cohesive sandstone analog to document four independent precursors of rock fracture over a range of stress conditions. These precursors can be employed with machine learning to predict the time and stress required to initiate a fracture. Our machine learning algorithm further reveals that failure prediction is improved by analyzing multiple precursors. Our findings suggest that to earthquake forecasting techniques may be improved by employing catalogs of individual precursors measuring the abundance, size, mechanism and spatial distribution of microcracks.

1. Introduction

Over the last couple of decades, seismologists have worked to improve earthquake prediction techniques by statistical analysis of earthquake foreshock, mainshock and aftershock sequences. Statistical variations in seismic event rate, seismic energy and moment preceding large earthquakes are observed widely but not systematically [Bouchon et al., 2013; Wyss, 1997; Cicerone et al. 2009]. Earthquakes have been suggested to be scale-independent, self-organized critical phenomenon [Main, 1996], thus, rock deformation experiments have been employed to understand the statistical variation in seismicity during slip along faults, before, during, and after earthquakes. Acoustic emissions (AE) recorded during biaxial and stick-slip experiments reveal accelerated and localized microcracking prior to failure [Amitrano, 2003; Lei and Satoh, 2007; Ojala et al., 2004; Rouet-Leduc et al., 2017], and associated decline in seismic *b-value*, which quantifies the proportion of small to large-magnitude microcracks [Rivière et al., 2018; Goebel et al., 2017]. Additionally, microcracking and associated acoustic energy release prior to rock failure are correlated with microcracking mode (tensile, shear and pore collapse) in granular rock [Fortin et al., 2006, 2009]. Several studies have quantified such individual precursory indicators of fracture and employed machine learning to predict failure in laboratory experiments. AE energy measurements during stick-slip experiments on granular media predict macroscopic fault properties such as shear stress, friction and time-to-failure using random forests [Rouet-Leduc et al., 2017; Lubbers et al., 2018; Corbi et al., 2019] and deep learning [Zhou et al., 2018]. These analyses provide insight into macroscopic fault properties, however, their applicability to predict fracture nucleation in cohesive materials over a range of confining pressures has not yet been demonstrated. Additionally, AE collected during biaxial deformation of intact crystalline rocks show the use of multiple independent precursory indicators (i.e. microcracking rate, location, source mechanism and moment) can improve failure prediction as they each exhibit unique temporal correlations with critical point [Lei et al., 2000, 2006]. Potentially, a holistic numerical examination of precursory signatures may help improve failure and earthquake forecasting techniques in rocks and along faults.

In this study, we use the Discrete Element Method [Cundall and Strack, 1979] to examine fracture growth during biaxial experiments on a calibrated sandstone model over a range of confining pressures. Fracture growth occurs through microcracking, which releases elastic energy analogous to acoustic emissions, in response to applied boundary stresses. By monitoring microcracking activity during simulated deformation experiments, we seek to constrain the various independent precursory signatures of shear fracture nucleation and rupture. We then use the calculated temporal precursory indicators with machine learning (ML) techniques to predict time-to-failure and stress-to-failure in our simulated experiments. Finally, we probe the results of our ML algorithm to test whether the use of multiple deformation indicators improves critical failure prediction.

2. Methods

We choose the Discrete Element Method to study the growth and nucleation of fractures because, much like real rocks, the numerical materials are composed of cohesive assemblages of particles. Interparticle bond breakage simulates microcracking, allowing us to study the distribution and mode of individual microcracks and associated elastic energy release [Vora and Morgan, 2019].

The interparticle mechanics of the code used here, RICEBAL, are described in detail by Vora and Morgan [2019]. We construct samples of dimension 0.0775 m x 0.038 m, consisting of ~6,000 bonded particles with particle diameters of 400 μm – 800 μm [Fig. S1], within the range of grain sizes observed in Berea sandstone [Churcher et al., 1991]. The samples are confined between horizontal walls, which act as flexible membranes imposing a specified confining pressure on the cohesive granular material. Axial compression is conducted by moving vertical platens inward at a constant velocity [Fig. S1]. As the lateral platens move inwards, local differential stresses increase, causing breakage of interparticle bonds and generating microcracks [Fig. 1a-c]. The coalescence of these microcracks ultimately results in the failure of the sample [Fig. 1d]. We simulate constant rate-of-strain ($2\text{x}10^{-6}$ m/s) biaxial experiments under confining pressures ranging from 0 to 50 MPa at increments of 5 MPa. All simulated biaxial experiments are conducted for a duration of 2000 model seconds, corresponding to a final axial strain (ε_a) of 10.3%.

During each simulated biaxial experiment, we document the applied axial stress and microcrack growth at time intervals of 20 seconds (ε_a interval of 0.1%).

The numerical materials used here are calibrated to match the geomechanical properties of Berea Sandstone. As described in Vora and Morgan [2019], the micromechanical model properties are adjusted incrementally, until the bulk behavior of our materials replicate experimental laboratory data for Berea Sandstone [Bobich, 2005; Schellart, 2000; Hart and Wang, 1995]. To capture the full range of geomechanical rock behavior, we reproduce experimentally derived elastic parameters such as Young's modulus (E) and Poisson's Ratio (v), and strength parameters such as Unconfined Compressive Strength (UCS), Mohr-Coulomb cohesion (C) and internal friction coefficient (μ). The calibration is explained in detail in supporting Text S1, Tables S1-S2, Fig. S1–S3.

Our goal is to quantify independent deformation indicators using local, moving time windows of microcracking data, and employ them to predict the critical point, defined as the peak stress condition during each biaxial test [Fig. 2a]. As axial stress is applied to the platens, interparticle bonds become distorted prior to failure, accumulating elastic strain energy. Bond failure that accompanies microcrack formation can occur in tensile and shear mode [Fig. 2a], releasing the elastic strain energy and emitting a signal analogous to an acoustic emission (AE) [Text S2a; Fig. S4]. AE from deformation experiments document that rupture is preceded by change in microcrack rate [Ojala et al., 2004], dominant microcracking mode [Fortin et al., 2009], spatial distribution of microcracks [Amitrano, 2003] and seismic moment [Lei and Satoh, 2007]. To characterize these temporal changes during rock deformation, we derive four independent, dimensionless deformation indicators using continuous, moving time window of 200 seconds (ε_a interval of 1.03%) [Fig. 2a]. The four deformation indicators are:

1. Microcracking Variance (MC_{var}), which quantifies the deviation from average microcracking rate during an experiment as

$$MC_{var} = \frac{1}{200}\sum_0^{200}|N_i - \mu_{MC}|^2 \quad , \tag{1}$$

where N_i is the number of microcracking events per second and μ_{MC} is the mean of number of microcracking rate within a time window ($\mu_{MC} = \frac{1}{200}\sum_0^{200} N_i$). The evolution of MC_{var} with axial strain provides a quantitative measure of temporal variations in microcracking rate during each biaxial experiment [Fig. 2b].

2. Shear Fraction (*SF*) of emergent microcracks by interparticle bond failure. The fraction of microcracks occurring in shear mode within each time window ($\sum_0^{200} N_{shear}$), is defined as

$$SF = \frac{\sum_0^{200} N_{shear}}{\sum_0^{200} N_i} \quad , \tag{2}$$

where $\sum_0^{200} N_i$ is the total number of microcracks occurring within a time window. The evolution of *SF* with axial strain provides a quantitative measure of temporal variations in microcracking mode during each biaxial experiment [Fig. 2b].

3. Seismic *b-value*, calculated as the slope of the AE moment-magnitude distribution within each time window [Fig. 2c] (details in supplementary Text S2a,b; Fig. S4-S6). Experimental AE moment distributions obey a power law relationship expressed by the Gutenberg-Richter law [Scholz, 1968], which we employ to calculate the seismic *b-value* within each time window as

$$b = \frac{a - \log(N_m)}{M} \quad , \tag{3}$$

where N_m is the number of microcrack clusters with moment greater than *M*, and *a* and *b* are the intercept and the slope of the frequency-magnitude relationship respectively [Text S2c; Fig. S7]. The *b-value* quantifies the proportion of small to large-magnitude microcracks, providing a quantitative measure of temporal variations in seismic moment during shear fracture growth [Fig. 2d].

4. Fractal Dimension of Microcrack Hypocenters (D_2), calculated as the slope of correlation integral ($C(R)$) with distance (R) [Text S3; Fig. S8]. We document the evolving location of microcracks [Fig. 1] and quantify their spatial distribution using the correlation integral ($C(R)$) [Hirata et al., 1987] as

$$C(R) = \frac{2}{N_p(N_p - 1)} N_r \quad (4)$$

for a set of N_p hypocenters, N_r is the number of pairs separated by a distance smaller than R. Assuming the distribution has a fractal structure, $C(R)$ is expressed by

$$C(R) \; \alpha \; R^{D_2} \quad , \quad (5)$$

where D_2 is the fractal dimension of microcrack hypocenters [Text S3; Fig. S8]. A low value of D_2 (~1) indicates localized microcracking in a sample; whereas, a high D_2 (~2) indicates distributed microcracking. The evolution of D_2 with axial strain provides a quantitative measure of temporal variations in microcrack distribution [Fig. 2d].

3. Results: Temporal Evolution of Deformation Indicators

To demonstrate our simulation results, we examine the growth of fractures in our sandstone analog under a confining pressure of 10 MPa, identifying indicators of critical failure during the experiment. Critical failure of the sample occurs at a peak stress of 117.72 MPa at t=600 s (ε_a=3.1%) during the biaxial experiment [Fig. 2a]. Experimental and numerical analyses show that the deformation process is characterized by four distinct phases of microcracking activity: Initiation, Nucleation, Rupture and Frictional Sliding [Renaud et al., 2017; Lei and Satoh, 2007; Vora and Morgan, 2019].

Stage 1 (initiation; t=0-440 s; ε_a=0-2.2%) is characterized by systematically increasing rock strength and nominal, distributed tensile microcracking [Fig. 2a; Fig. 1a]. The initiation phase reflects initial distributed microcracking and rupture of pre-existing asperities. We calculate low magnitudes of indicators MC_{var} and SF [Fig. 2b], narrow range of seismic moment [Fig. 2c], and high magnitudes of *b-value* and D_2 [Fig. 2d] associated with this early stage of fracture initiation.

Stage 2 (nucleation; *t*=440-600 s; ε_a=2.2-3.1%) is characterized by peak rock strength [Fig. 2a] and accelerated, localized microcracking [Fig. 2a; Fig 1b]. The nucleation phase involves sub-critical growth of the microcrack population. We document the following precursors of critical failure: (a) high microcracking activity and an increase of over two orders of magnitude in MC_{var} [Fig. 2b], (b) peak magnitude of *SF* occurring prior to critical point [Fig. 2b], (c) large acoustic energy and wide range of seismic moments [Fig. 2c; Fig. S5b], and a resultant precursory decline in seismic *b-value* prior to critical failure [Fig. 2d], and (d) localized microcracking resulting in a precursory decline in D_2 prior to critical failure [Fig. 1b; Fig. 2d].

Stage 3 (rupture; *t*=600-1100 s; ε_a=3.1-5.6%) is characterized by declining rock strength and high microcracking [Fig. 2a]. The rupture phase corresponds to microcrack coalescence along one or more incipient fracture planes [Fig. 1c]. We calculate a post-failure decline in MC_{var} and *SF* [Fig. 2b], decline in range of seismic moment [Fig. 2c], and post-failure rebound to relatively constant magnitude of seismic *b-value* and D_2 [Fig. 2d].

Stage 4 (frictional sliding) corresponding to *t*=1100-2000 s (ε_a=5.7-10.3%) is characterized by residual stress and very low microcracking [Fig. 2a]. The frictional sliding phase represents the sliding of fault blocks along the developed fracture planes and associated microcracking in gouge [Fig. 1d]. We calculate very low magnitudes of *MCvar* and *SF* [Fig. 2b], narrow range of seismic moments [Fig. 2c], and relatively constant magnitudes of *b-value* and D_2 [Fig. 2d].

Each documented deformation indicator demonstrates distinct precursory time-to-failure characteristics during simulated biaxial experiments on the sandstone analog. Over confining pressures of 0-50 MPa, we document the following precursors of failure: 1) increase in MC_{var} of one to two orders of magnitude, 2) peak *SF* ranging from 0.15 to 0.95, 3) a decline in D_2 from 1.65–1.85 to 1.35–1.55 at critical point, and 4) a decline in *b-value* from 1.4–2.3 to 0.8–1.3 at critical point [Fig. 2; Fig. S9-S13]. The precursory increase in MC_{var} and *SF* is due to accelerated microcracking prior to critical point especially in shear mode [Fig. 2a; Fig. 2b], analogous to microcracking observed in sandstone samples prior to rupture [Fortin et al., 2009; Ojala et al., 2004; Baud et al., 2015; Mair et al., 2002]. The precursory decline in D_2 and *b-value* is due to localization of microcracking along an emergent fracture plane [Fig. 1b; Fig. 2d] and an increase in range of AE moment prior to critical failure [Fig. 2c,d], analogous to laboratory observations of AE [Amitrano, 2003; Lei and Satoh, 2007; Rivière et al., 2018; Goebel et al., 2017]. Thus, we provide a novel integrated analysis of deformation indicators utilizing microcracking rate, mode, spatial distribution and moment during deformation of sandstone analogs over a range of confining pressures (0-50 MPa).

4. Failure Prediction using Artificial Neural Networks

We employ the calculated temporal trends of deformation indicators to quantitatively predict critical failure in cohesive granular rock material. Recently, machine learning techniques have been employed to forecast failure from laboratory rock deformation experiments to earthquakes [Corbi et al., 2019; Rouet-Leduc et al., 2017; Dou et al., 2015; Panakkat and Adeli, 2009; Lubbers et al., 2018]. For this study, we use artificial neural networks (ANN), a network of quantitative pattern recognition functions that are suitable for failure prediction due to their mathematical non-linearity, error tolerance and their ability to incorporate inputs across different physical units and magnitudes. We develop an ANN to predict time-to-failure (*TTF*) and stress-to-failure (*STF*) for the biaxial tests of sandstone analogs described above and determine the relative importance of these deformation indicators. *TTF* and *STF* are defined as

$$TTF = t - t^{max} \quad , \qquad (5)$$

$$STF = \begin{cases} \sigma_a - \sigma_a^{max}, \ TTF < 0 \\ \sigma_a^{max} - \sigma_a, \ TTF > 0 \end{cases} \quad , \qquad (6)$$

where t^{max} is the time at critical point and σ_a^{max} is the axial stress at the critical point of a biaxial experiment. Thus, negative values of *TTF* and *STF* correspond to pre-failure stages (initiation and nucleation), positive values of *TTF* and *STF* indicate post-failure stages (rupture and frictional sliding), and *TTF*=0 and *STF*=0 correspond to critical failure. In our study, we use a particular type of ANN model, known as a Multi-Layer Perceptron (MLP).

The MLP is a feed-forward neural network with the goal of approximating an arbitrary function between the inputs (deformation indicators and confining pressure) and outputs (*TTF* and *STF*) [Fig. S14]. In MLP's, information flows through three layers: input (*layer x*), hidden (*layer y*) and output (*layer z*). Each layer has its corresponding neurons and weights, and the outputs are deterministically computed by iteratively by iteratively optimizing synaptic weights w_{xy} (between input and hidden layers) and w_{yz} (between hidden and output layers) to optimize fit to desired target values [Text S4a; Fig. S14-S15]. The MLP inputs are the derived deformation indicators (MC_{var}, *SF*, D_2 and *b-value*) and confining pressure (*CP*) from nine biaxial tests under confining pressures of 0, 5,10,15,20,30,35,40 and 45 MPa, with 70% randomly allocated for training and the remaining 30% allocated for testing [Text S4b]. We conduct two "blind tests" to check the prediction performance of the MLP for datasets it is not trained upon. During "blind tests", the MLP is fed microcracking indicators during biaxial tests conducted under confining pressures of 25 MPa (lying within range of confining pressures used for MLP training) and 50 MPa (lying outside range of confining pressures used for MLP training) and predicts values for *TTF* and *STF*. To quantify the quality of the predictions, we report the correlation coefficient R^2.

4.1. Failure Prediction Results

Over the training and testing dataset (deformation indicators from simulated biaxial tests under confining pressures of 0, 5, 10, 15, 20, 30, 35, 40, and 45 MPa), our MLP shows good correlation between multivariate deformation indicators and target time-to-failure (*TTF*) (training R^2= 0.86; testing R^2=0.83) and target stress-to-failure (*STF*) (training R^2= 0.95; testing R^2=0.90) [Fig. 3; Fig. S16]. The predicted values *TTF* and *STF* during training and testing show a reasonable match with target data, with the predictions improving for biaxial tests conducted at higher confining stresses of 15-45 MPa [Fig. 3]. Additionally, "blind test" predictions of *TTF* and *STF* for tests under confining pressures of 25 MPa and 50 MPa show good correlation with target values (*TTF* prediction R^2=0.96 and 0.51 respectively; *STF* prediction R^2=0.92 and 0.39 respectively) [Fig. 3].

The predictions of *TTF* and *STF* using our MLP exhibit better fit to target values as we approach critical point for each experiment. Pre-failure *TTF* and *STF* predictions corresponding to $t \approx$ 200 s - 600 s show weaker correlation with target values [Fig. 3] due to low microcracking activity during fracture initiation stage [Fig 2]. Post-failure *TTF* and *STF* predictions corresponding to $t \approx$ 1660 s – 2000 s show weaker correlation with target values [Fig. 3] due to indistinct trends of indicators during the frictional sliding stage of experiments [Fig. 2]. *TTF* and *STF* predictions using our MLP improve at higher confining pressures (15-50 MPa) due to increased microcracking and sharper precursory changes in deformation indicators prior to critical point at higher confining pressures [Fig. S9-S13]. The correlation between predictions and targets (*TTF* and *STF*) during the “blind tests” exhibits the versatility of our machine learning approach to predict failure over a range of confining pressures [Fig. 3]. Overall, our MLP exhibits strong capability to predict time-to-failure and stress-to-failure using deformation indicators in our sandstone analog over confining pressures of 0-50 MPa.

4.2. Relative Importance of Damage Indicators

We employ the validated prediction capability of our MLP to quantify the importance of individual indicators for failure prediction. The MLP iteratively finds correlations between the input deformation indicators and outputs (*STF* and *TTF*) by iteratively assigning weights to the set of nodes and connections [Fig. S14], which quantify the predictive capability of each deformation indicator. We investigate the weights assigned to nodes of the MLP to understand the relative importance of each input feature [Garson, 1991] as

$$I_x = \sum_{x=1}^{n} \frac{|w_{xy} w_{yz}|}{\sum_{y=1}^{m} |w_{xy} w_{yz}|} , \quad (7)$$

$$RI_x = \frac{I_x}{\sum_{x=1}^{n} I_x} * 100 \quad , \quad (8)$$

where I_x is the importance of input *x*, *n* is the number of inputs (*n*=5), *m* is the number of hidden neurons (*m*=5), $\sum_{y=1}^{m} |w_{xy} w_{yz}|$ is the sum of product of the final weights of the connections from input neurons to the hidden neurons (w_{xy}) with the connections from the hidden neurons to the output neurons (w_{yz}), and RI_x (%) is the relative importance of input x.

Over 50 MLP initializations, we calculate a *RI* of 15.4%-26.8% for time-to-failure (*TTF*) prediction, and 8.5%-24.3% for stress-to-failure (*STF*) prediction for the five inputs into the MLP [Table 1; Tables S3, S4].Our results show that microcracking variance (MC_{var}) and fractal dimension (D_2) are the most important *TTF* predictors, whereas shear fraction (*SF*) and seismic *b-value* are the most important *STF* predictors [Table 1; Tables S3,S4]. Thus, our models suggest that rapid and localized microcracking during fracture nucleation is the strongest precursor to critical failure in the time domain, whereas the transition to shear microcracking and increase in range of seismic moments during fracture nucleation are strongest precursors of critical stress. Overall, our machine learning algorithm indicates that all four deformation indicators (MC_{var}, *SF*, D_2 and *b-value*) improve fit to target values, indicating the importance for an integrated analysis with multiple indicators for failure prediction. We document improved failure prediction capability than experimental analyses of Rouet-Leduc et al. [2017] and Lubbers et al. [2018], perhaps due to the deterministic nature of our numerical models, and the use of multiple deformation indicators as inputs in our machine learning algorithm.

4.3. Geophysical Implication of Failure Prediction

The study of rock failure is of widespread interest, with relevance to both artificial applications such as geothermal recovery, oil production, safe design of nuclear repositories, and natural processes such as volcanism and earthquake prediction. In this study, we have used a numerical sandstone analog to document four independent precursors to rock failure using microcracking rate, mode, location and moment distribution over a range of confining pressures [Fig. 2]. Furthermore, we show that the use of multiple temporal precursors with machine learning provides robust, quantitative failure prediction [Fig. 3]. Several studies have documented similar precursors to large earthquakes, such as increase in foreshocks and radiated seismic energy [Meredith et al., 1990; Reasenberg, 1999], temporal variations in focal mechanisms in earthquake sequences [Reasenberg, 1999; Scholz, 2019], decline in fractal dimension of earthquake epicenters [Enescu and Ito, 2001; Kagan and Jackson, 1991], and decline in seismic b-values [Meredith et al., 1990; Nuannin et al., 2005]. Our results suggest that integrated catalogs documenting the temporal variations in foreshock rate, energy, focal mechanism, source location and seismic moments can be employed with machine learning techniques to improve short-term earthquake forecasting techniques.

5. Conclusions

We document the growth of shear fractures during simulated biaxial tests on calibrated numerical analogs of sandstone under confining pressures of 0-50 MPa. We track the abundance, location and seismic moment associated with emergent microcracks to derive four scale-independent deformation indicators – variance of microcracking (MC_{var}), fraction of microcracks in shear mode of total microcracks (*SF*), fractal dimension of microcrack hypocenters (D_2) and slope of the frequency-magnitude moment distribution (*b-value*). Over confining pressures of 0-50 MPa, each deformation indicator shows typical time-to-failure characteristics. Pre-failure microcracking is characterized by 1) increase in MC_{var} of one to two orders of magnitude, 2) peak *SF* ranging from 0.15 to 0.95, 3) a decline in D_2 from 1.65–1.85 to 1.35–1.55 at critical point, and 4) a decline in *b-value* from 1.4–2.3 to 0.8–1.3 at critical point.

We employ the temporal trends of the calculated microcracking indicators and confining pressure as inputs into multilayer perceptron (MLP) to predict time-to-failure and stress-to-failure in our sandstone analog. Over confining pressures of 0-50 MPa, our MLP predicts time-to-failure and stress-to-failure well (R^2 of 0.85 and 0.95 respectively). Our machine learning results suggest that all four deformation indicators (MC_{var}, *SF*, D_2 and *b-value*) improve critical failure prediction, indicating the importance for an integrated analysis of precursory signals. Thus, we show that an integrated analysis of multiple scale-independent precursory indicators can be utilized with machine learning to quantitatively predict critical failure in cohesive rock material.

Acknowledgements: This work has been funded in part by fellowships to Harsh Biren Vora from the Department of Earth, Environment and Planetary Science, Rice University. Computing facilities were made available through the Center for Computational Geophysics. The authors benefitted from discussions on numerical modeling with David Blank. Modeling results and information can be obtained in supporting information and at https://figshare.com/projects/GRL_-_DEM_with_Machine_Learning/67529.

References

Amitrano, D. (2003), Brittle-ductile transition and associated seismicity: Experimental and numerical studies and relationship with the *b* value, *J. Geophys. Res. Solid Earth*, *108*(B1), 1–15, doi:10.1029/2001JB000680.

Basheer, I. A., & Hajmeer, M. (2000). Artificial neural networks: fundamentals, computing, design, and application. *Journal of microbiological methods*, *43*(1), 3-31.

Baud, P., Reuschlé, T., Ji, Y., Cheung, C. S., & Wong, T. F. (2015). Mechanical compaction and strain localization in Bleurswiller sandstone. *Journal of Geophysical Research: Solid Earth*, *120*(9), 6501-6522.

Boettcher, M. S., A. McGarr, and M. Johnston (2009), Extension of Gutenberg-Richter distribution to Mw -1.3, no lower limit in sight, *Geophys. Res. Lett.*, *36*(10), 1–5, doi:10.1029/2009GL038080.

Bonnet, E., Bour, O., Odling, N. E., Davy, P., Main, I., Cowie, P., & Berkowitz, B. (2001). Scaling of fracture systems in geological media. *Reviews of geophysics*, *39*(3), 347-383.

Bouchon, M., V. Durand, D. Marsan, H. Karabulut, and J. Schmittbuhl (2013), The long precursory phase of most large interplate earthquakes, *Nat. Geosci.*, *6*(4), 299–302, doi:10.1038/ngeo1770.

Churcher, P. L., P. R. French, J. C. Shaw, and L. L. Schramm (2007), Rock Properties of Berea Sandstone, Baker Dolomite, and Indiana Limestone, , (February 1991), doi:10.2118/21044-ms.

Cicerone, R. D., J. E. Ebel, and J. Britton (2009), A systematic compilation of earthquake precursors, *Tectonophysics*, *476*(3–4), 371–396, doi:10.1016/j.tecto.2009.06.008.

Cook, B. K., Lee, M. Y., DiGiovanni, A. A., Bronowski, D. R., Perkins, E. D., & Williams, J. R. (2004). Discrete element modeling applied to laboratory simulation of near-wellbore mechanics. *International Journal of Geomechanics*, *4*(1), 19-27.

Corbi, F., L. Sandri, J. Bedford, F. Funiciello, S. Brizzi, M. Rosenau, and S. Lallemand (2019), Machine Learning Can Predict the Timing and Size of Analog Earthquakes, *Geophys. Res. Lett.*, *46*(3), 1303–1311, doi:10.1029/2018GL081251.

Cundall, P. A., and O. D. L. Strack (1979), A discrete numerical model for granular assemblies, *Géotechnique*, *29*(1), 47–65, doi:10.1680/geot.1979.29.1.47.

Dou, J., H. Yamagishi, H. R. Pourghasemi, A. P. Yunus, X. Song, Y. Xu, and Z. Zhu (2015), An integrated artificial neural network model for the landslide susceptibility assessment of Osado Island, Japan, *Nat. Hazards*, *78*(3), 1749–1776, doi:10.1007/s11069-015-1799-2.

Enescu, B., and K. Ito (2001), Some premonitory phenomena of the 1995 Hyogo-Ken Nanbu (Kobe) earthquake: Seismicity, b-value and fractal dimension, *Tectonophysics*, *338*(3–4), 297–314, doi:10.1016/S0040-1951(01)00085-3.

Fortin, J., S. Stanchits, G. Dresen, and Y. Guéguen (2006), Acoustic emission and velocities associated with the formation of compaction bands in sandstone, *J. Geophys. Res. Solid Earth*, *111*(10), 1–16, doi:10.1029/2005JB003854.

Fortin, J., S. Stanchits, G. Dresen, and Y. Gueguen (2009), Acoustic emissions monitoring during inelastic deformation of porous sandstone: Comparison of three modes of deformation, *Pure Appl. Geophys.*, *166*(5–7), 823–841, doi:10.1007/s00024-009-0479-0.

Felzer, K. R. (2006, December). Calculating the Gutenberg-Richter b value. In *AGU Fall Meeting Abstracts*.

Garson, G. D. (1991), Interpreting neural-network connection weights. *AI expert*, *6*(4), 46-51.

Goodfellow, I., Bengio, Y., & Courville, A. (2016). *Deep learning*. MIT press.

Goebel, T. H. W., G. Kwiatek, T. W. Becker, E. E. Brodsky, and G. Dresen (2017), What allows seismic events to grow big?: Insights from b-value and fault roughness analysis in laboratory stick-slip experiments, *Geology*, *45*(9), 815–818, doi:10.1130/G39147.1.

Hart, D. J., & Wang, H. F. (1995). Laboratory measurements of a complete set of poroelastic moduli for Berea sandstone and Indiana limestone. *Journal of Geophysical Research: Solid Earth*, *100*(B9), 17741-17751.

Hazzard, J. F., and R. P. Young (2000), Simulating acoustic emissions in bonded-particle models of rock, *Int. J. Rock Mech. Min. Sci.*, *37*(5), 867–872, doi:10.1016/S1365-1609(00)00017-4.

Hirata, T., T. Satoh, and K. Ito (1987), Fractal structure of spatial distribution of microfracturing in rock Takayuki Hirata, *Geophys. J. R. astr. Soc.*, (May 2018), 369–374.

Kagan, Y. Y., and D. D. Jackson (1991), Long-Term Earthquake Clustering, *Geophys. J. Int.*, *104*(1), 117–134, doi:10.1111/j.1365-246X.1991.tb02498.x.

Kanamori, H. (1983), Magnitude scale and quantification of earthquakes, *Tectonophysics*, *93*(3–4), 185–199, doi:10.1016/0040-1951(83)90273-1.

Kanamori, H., and L. Rivera (2006), Energy partitioning during an earthquake, *Geophys. Monogr. Ser.*, *170*, 3–13, doi:10.1029/170GM03.

Lei, X., and T. Satoh (2007), Indicators of critical point behavior prior to rock failure inferred from pre-failure damage, *Tectonophysics*, *431*(1–4), 97–111, doi:10.1016/j.tecto.2006.04.023.

Lei, X., K. Kusunose, M. V. M. S. Rao, O. Nishizawa, and T. Satoh (2000), Quasi-static fault growth and cracking in homogeneous brittle rock under triaxial compression using acoustic emission monitoring, *J. Geophys. Res. Solid Earth*, *105*(B3), 6127–6139, doi:10.1029/1999JB900385.

Lockner, D. (1993), The role of acoustic emission in the study of rock fracture, *Int. J. Rock Mech. Min. Sci.*, *30*(7), 883–899, doi:10.1016/0148-9062(93)90041-B.

Lubbers, N., D. C. Bolton, J. Mohd-Yusof, C. Marone, K. Barros, and P. A. Johnson (2018), Earthquake Catalog-Based Machine Learning Identification of Laboratory Fault States and the Effects of Magnitude of Completeness, *Geophys. Res. Lett.*, *45*(24), 13,269-13,276, doi:10.1029/2018GL079712.

Madariaga, R. (1976). Dynamics of an expanding circular fault. *Bulletin of the Seismological Society of America*, *66*(3), 639-666.

Madden, E. H., M. L. Cooke, and J. McBeck (2017), Energy budget and propagation of faults via shearing and opening using work optimization, *J. Geophys. Res. Solid Earth*, *122*(8), 6757–6772, doi:10.1002/2017JB014237.

Main, I. (1996). Statistical physics, seismogenesis, and seismic hazard. *Reviews of Geophysics*, *34*(4), 433-462.

Mair, K., S. Elphick, and I. Main (2002), Influence of confining pressure on the mechanical and structural evolution of laboratory deformation bands, *Geophys. Res. Lett.*, *29*(10), 49-1-49–4, doi:10.1029/2001gl013964.

Mavko, G., Mukerji, T., & Dvorkin, J. (2009). The rock physics handbook: Tools for seismic analysis of porous media. Cambridge university press.

Meredith, P. G., I. G. Main, and C. Jones (1990), Temporal variations in seismicity during quasi-static and dynamic rock failure, *Tectonophysics*, *175*(1–3), 249–268, doi:10.1016/0040-1951(90)90141-T.

Nuannin, P., O. Kulhanek, and L. Persson (2005), Spatial and temporal b value anomalies preceding the devastating off coast of NW Sumatra earthquake of December 26, 2004, *Geophys. Res. Lett.*, *32*(11), 1–4, doi:10.1029/2005GL022679.

Ojala, I. O., I. G. Main, and B. T. Ngwenya (2004), Strain rate and temperature dependence of Omori law scaling constants of AE data: Implications for earthquake foreshock-aftershock sequences, *Geophys. Res. Lett.*, *31*(24), 1–5, doi:10.1029/2004GL020781.

Okal, E. A., and B. A. Romanowicz (1994), On the variation of b-values with earthquake size, *Phys. Earth Planet. Inter.*, *87*(1–2), 55–76, doi:10.1016/0031-9201(94)90021-3.

Panakkat, A., and H. Adeli (2009), Recurrent neural network for approximate earthquake time and location prediction using multiple seismicity indicators, *Comput. Civ. Infrastruct. Eng.*, *24*(4), 280–292, doi:10.1111/j.1467-8667.2009.00595.x.

Reasenberg, P. A. (1999), Foreshock occurrence before large earthquakes, *J. Geophys. Res. Solid Earth*, *104*(B3), 4755–4768, doi:10.1029/1998jb900089.

Renard, F., B. Cordonnier, M. Kobchenko, N. Kandula, J. Weiss, and W. Zhu (2017), Microscale characterization of rupture nucleation unravels precursors to faulting in rocks, *Earth Planet. Sci. Lett.*, *476*, 69–78, doi:10.1016/j.epsl.2017.08.002.

Rivière, J., Z. Lv, P. A. Johnson, and C. Marone (2018), Evolution of b-value during the seismic cycle: Insights from laboratory experiments on simulated faults, *Earth Planet. Sci. Lett.*, *482*, 407–413, doi:10.1016/j.epsl.2017.11.036.

Rouet-Leduc, B., C. Hulbert, N. Lubbers, K. Barros, C. J. Humphreys, and P. A. Johnson (2017), Machine Learning Predicts Laboratory Earthquakes, *Geophys. Res. Lett.*, *44*(18), 9276–9282, doi:10.1002/2017GL074677.

Schellart, W. P. (2000), Shear test results for cohesion and friction coefficients for different granular materials: Scaling implications for their usage in analogue modelling, *Tectonophysics*, *324*(1–2), 1–16, doi:10.1016/S0040-1951(00)00111-6.

Scholtès, L., and F. V. Donzé (2013), A DEM model for soft and hard rocks: Role of grain interlocking on strength, *J. Mech. Phys. Solids*, *61*(2), 352–369, doi:10.1016/j.jmps.2012.10.005.

Scholz, C. H. (1968). The frequency-magnitude relation of microfracturing in rock and its relation to earthquakes. *Bulletin of the seismological society of America*, *58*(1), 399-415.

Scholz, C. H. (2019). *The mechanics of earthquakes and faulting*. Cambridge university press, Cambridge.

Tang, C. A., and P. K. Kaiser (1998), Numerical Simulation of Cumulative Damage and Seismic Energy Release During Brittle Rock Failure—Part I: Fundamentals, *Int. J. Rock Mech. Min. Sci.*, *35*(2), 113–121, doi:10.1016/S0148-9062(97)00009-0.

van der Baan, M., and C. Jutten (2002), Neural networks in geophysical applications, *Geophysics*, *65*(4), 1032–1047, doi:10.1190/1.1444797.

Vora, H. B., & Morgan, J. K. Microscale Characterization of Fracture Growth and Associated Energy in Granite and Sandstone Analogs: Insights using the Discrete Element Method. *Journal of Geophysical Research: Solid Earth*.

Wang, B., Y. Chen, and T. Wong (2008), A discrete element model for the development of compaction localization in granular rock, , *113*(December 2007), 1–17, doi:10.1029/2006JB004501.

Wang, Y., & Tonon, F. (2011). Discrete element modeling of rock fragmentation upon impact in rock fall analysis. Rock mechanics and rock engineering, 44(1), 23-35.

Wyss, M. (1997), I Pure and Applied Geophysics Second Round of Evaluations of Proposed Earthquake Precursors, *Pure appl. Geophys*, *149*(3).

Zhou, Z., Lin, Y., Zhang, Z., Wu, Y., & Johnson, P. (2019). Earthquake Detection in 1D Time-Series Data with Feature Selection and Dictionary Learning. *Seismological Research Letters*, *90*(2A), 563-572.

Tables

Table 1: Relative Importance of MLP inputs calculated from connection weights.

Indicator	Relative Importance (*RI*) for Time-to-Failure Prediction (%)	Relative Importance (*RI*) for Stress-to-Failure Prediction (%)
Microcracking Variance (MC_{var})	26.82	21.32
Shear Fraction (*SF*)	15.71	24.29
Fractal Dimension of Microcracks (D_2)	17.57	23.29
Seismic *b-value*	24.50	22.61
Confining Pressure (*CP*)	15.38	8.47

Figure Captions

Figure 1: The growth of shear fracture occurs through the coalescence of shear and tensile microcracks during biaxial test under confining pressure of 10 MPa, sampled at times of (a) 400 s, (b) 720 s, (c) 1200 s, and (d) 1800 s.

Figure 2: Evolution of microcracking and deformation indicators in sandstone analog during biaxial test under confining pressure of 10 MPa. (a) Applied axial stress and microcracking in shear and tensile modes documented as a function of axial strain. Strain markers 1-4 indicate onset of stages of deformation and correspond to fracture initiation (t=400 s), nucleation (t=720 s), rupture (t=1200 s) and frictional sliding (t=1800 s), complementing the microcrack distributions in Fig. 1. (b) Microcrack variance (MC_{var}) and shear fraction (*SF*) exhibit precursory increase in magnitude prior to critical failure (c) Calculated increase in range of seismic moment magnitudes prior to critical failure. The central circle on each box indicates median moment magnitude; bottom and top edges of the box indicate 25th and 75th percentiles, respectively. The whiskers extend to the most extreme data points not considered statistical outliers; outliers are plotted individually as 'o' symbols. (d) Seismic *b-value* and fractal dimension of microcrack location (D_2) exhibit precursory decline prior to critical failure.

Figure 3: Regression performance for the MLP using inputs of confining pressure and deformation indicators from sandstone analog. MLP shows good capability to predict time-to-failure (*TTF*) and stress-to-failure (*STF*) during training and testing for nine simulated experiments, and “blind test” predictions for two simulated experiments.

Figure 1.

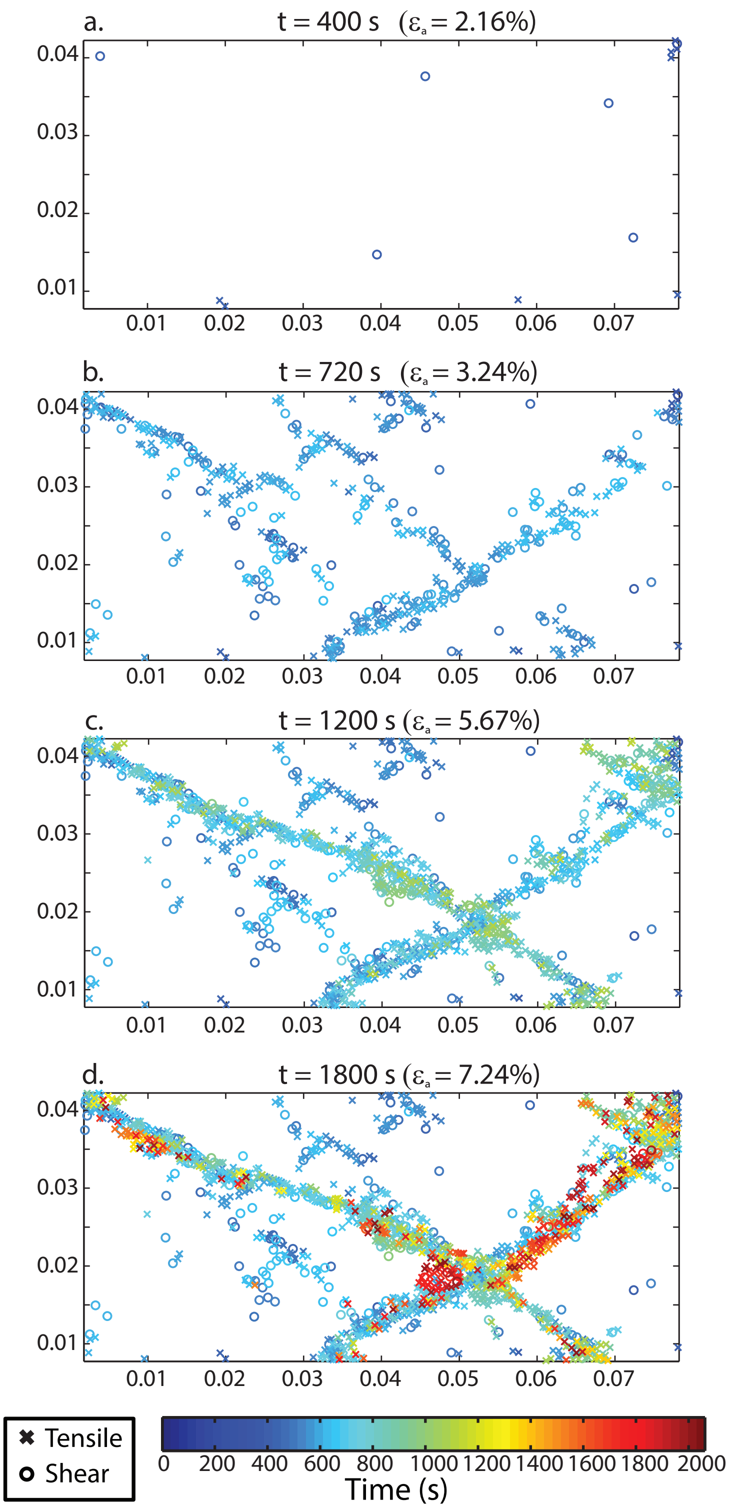
a. t = 400 s (ε_a = 2.16%)
b. t = 720 s (ε_a = 3.24%)
c. t = 1200 s (ε_a = 5.67%)
d. t = 1800 s (ε_a = 7.24%)
0.01
0.02
0.03
0.04
0.05
0.06
0.07
Tensile
Shear
0
200
400
600
800
1000
1200
1400
1600
1800
2000
Time (s)

Figure 2.

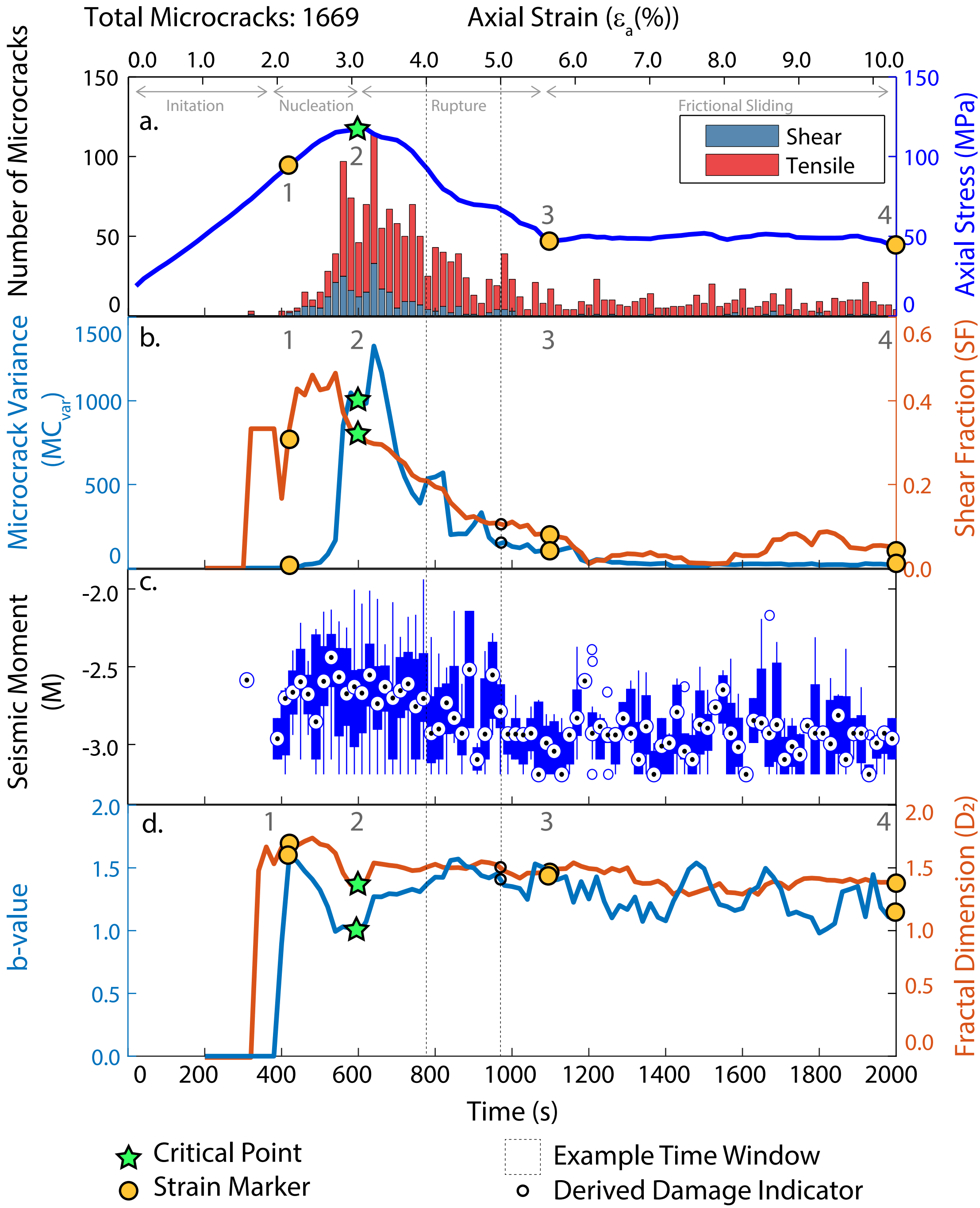
Total Microcracks: 1669
Axial Strain (ε_a(%))
0.0 1.0 2.0 3.0 4.0 5.0 6.0 7.0 8.0 9.0 10.0
Initation
Nucleation
Rupture
Frictional Sliding
a.
Shear
Tensile
Number of Microcracks
Axial Stress (MPa)
b.
Microcrack Variance (MC_var)
Shear Fraction (SF)
c.
Seismic Moment (M)
d.
b-value
Fractal Dimension (D₂)
Time (s)
Critical Point
Strain Marker
Example Time Window
Derived Damage Indicator

Figure 3.

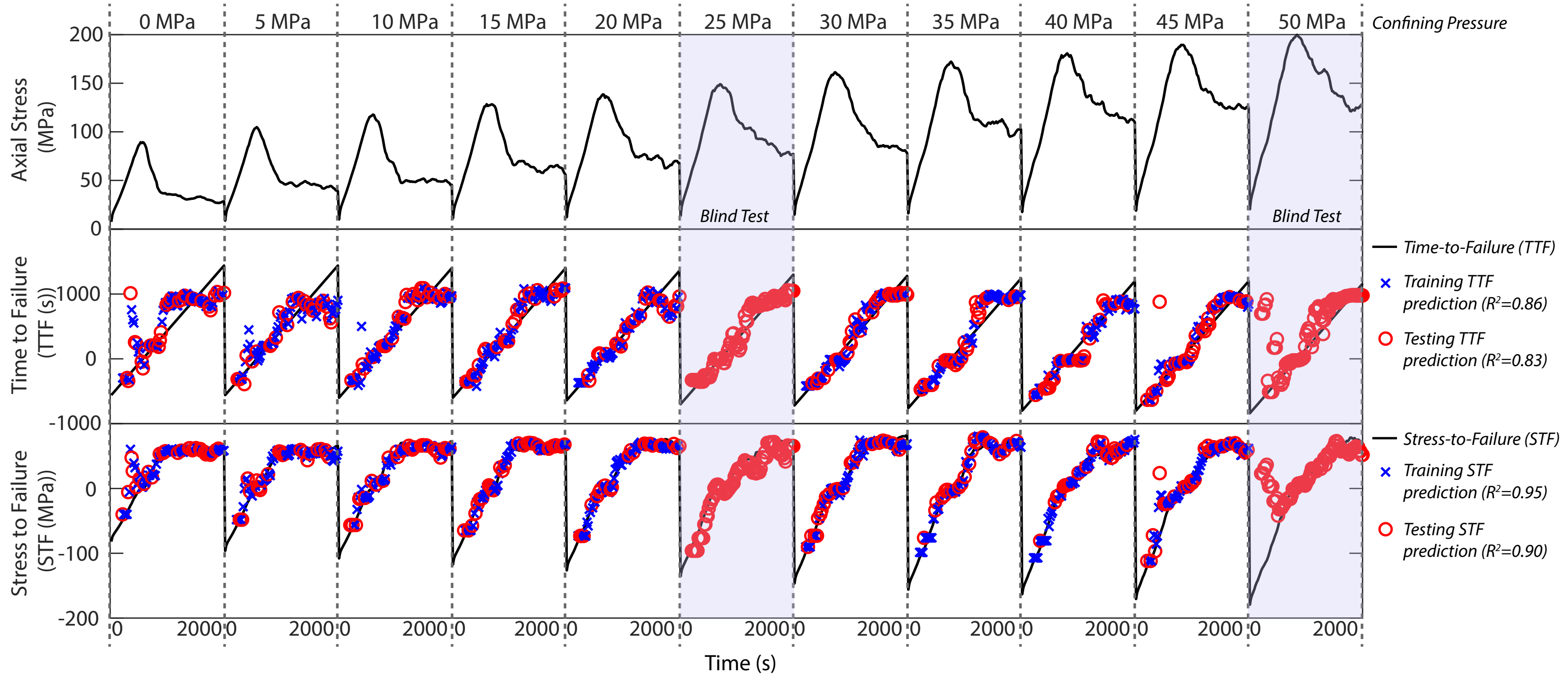

0 MPa
5 MPa
10 MPa
15 MPa
20 MPa
25 MPa
30 MPa
35 MPa
40 MPa
45 MPa
50 MPa
Confining Pressure
Axial Stress (MPa)
Blind Test
Blind Test
Time to Failure (TTF (s))
Time-to-Failure (TTF)
Training TTF prediction (R^2=0.86)
Testing TTF prediction (R^2=0.83)
Stress to Failure (STF (MPa))
Stress-to-Failure (STF)
Training STF prediction (R^2=0.95)
Testing STF prediction (R^2=0.90)
Time (s)